# Finite-Element simulations of Ribs subjected to dynamic three point bending loads

Aravind Rajan Ayagara, André Langlet, Ridha Hambli

# Finite-Element simulations of Ribs subjected to dynamic three point bending loads

## Aravind Rajan Ayagara[a], André Langlet[b], Ridha Hambli[c]

a. Laboratoire de Mécanique Gabiel Lamé, Université d'Orléans :
aravind-rajan.ayagara@univ-orleans.fr

b. Laboratoire de Mécanique Gabiel Lamé, Université d'Orléans : andre.langlet@univ-orleans.fr

c. Laboratoire de Mécanique Gabiel Lamé, Université d'Orléans : ridha.hambli@univ-orleans.fr

## Résumé :

*Nous proposons un modèle éléments-finis avec comportement élastique viscoplastique couplé à une loi d'endommagement incrémentale, dépendante de l'état de contrainte . La géométrie tridimensionnelle de la côte a été reconstruite à partir des contours des images DICOM obtenu par la tomographie quantitative (HR-pQCT). La masse volumique apparente est corrélée aux intensités de niveaux de gris par une relation linéaire. Les résultats des simulations ont été validés par les données expérimentales obtenues lors d'essais de flexion avec le système des barres de Hopkinson. Le modèle de EF proposé permet de prédire de manière satisfaisante l'occurrence de la fracture et sa propagation.*

## Abstract :

*Rib fractures due to a blunt impact to the chest pose a huge risk today. In order to mitigate these effects, it is necessary to understand the mechanical behavior of ribs under similar mechanical environments. We propose a Finite Element with elasticviscoplastic constitutive coupled to an external damage law. The three-dimensional rib geometry was generated from the contours of DICOM images of High-Resolution peripheral Quantitative Computed Tomography (HR-pQCT) scans. Apparent dry density was correlated to grey scale intensities through a linear relationship. The mechanical properties for bone constituents based on apparent density, gave the best results. The FE results were validated by experimental data obtained from Split Hopkinson Pressure bar tests. The proposed FE model was able to predict satisfactory force-displacement response and fracture pattern.*

**Mots clefs : Blunt impact, Porcine ribs, HR-pQCT, Dynamic response, Split Hopkinson Pressure Bar, Finite Element simulations, LS-Dyna.**

# 1  Introduction

The bone fragments originating from a blunt thoracic impact pose a risk of penetration thereby causing complex medical conditions, for example, pneumothorax, hemothorax or sometimes even a fail chest leading to eventual death. Therefore, trauma to the chest is one of the main contributors to the development of medical complexity and even mortality among polytrauma patients [1]. A recent study on chest trauma proposed by [2] states that a chest trauma can be caused either by a blunt impact or a penetrating impact. As the projectile does not penetrate into the body, an blunt impact cannot be identified as easily as a penetrating impact. Therefore, the blunt trauma (a trauma to the chest by blunt impact) needs more attention and time for recovery [2],[3]. Another aspect of blunt trauma is that the injury mechanism does play an important role [4],[5]. Among which road traffic accidents are the most commonly encountered injury mechanisms, which are important to be known prior to a radiological examination. Therefore, we are interested to understand the behavior of rib under blunt impact environment.

The advantages of FE simulations over expensive and time staking experimental procedures (e.g. human dummies) have drawn attention for years now. Several numerical human thorax models are have been developed : Isolated thorax models [6], H-model [7], RADIOSS [8], THUMS [9], and HUMOS [10]. Despite their efficiency and frequent use, these FE models still have some constraints, such as : geometrical representation, use elements, constitutive law, and damage law. To understand the behavior of ribs under such environment, the mechanical properties, the geometrical representation, the constitutive behavior and progressive nature of damage must be given equal importance.

Quite a lot of researches can be found on the mechanical properties of bones and the properties influencing them through regressions. We can notice that some authors consider both cortical and trabecular bone are formed by same morphological tissue *i.e.* the tissue density of both bones is the same and the difference in mechanical behavior is due to the architectural arrangements. While other authors state that they both are of different morphological tissue. Therefore, leading to the use of different independent variables. These studies can be categorized in terms of the independent variable used. For example, the apparent density $\rho_{app}$ was considered by [11],[12] and [13]. In contrast to $\rho_{app}$, mineralization based parameters such as ash fraction $\alpha$ or apparent ash density $\rho_{\alpha}$ were also considered as independent variables. Some researches regarding the later are [14],[15]. One of the recent studies on the parameters influencing bone properties put forth by [16] had considered both volume fraction $V_f$ and ash fraction $\alpha$. They had stated the bone tissue density $\rho_{tissue}$ is influenced by its mineralization and had proposed regression formulae.

Apart from the aforementioned variables, there are variables that influence the mechanical behavior of bones. One of the most important variables influencing the mechanical behavior of bones is the strain rate $\dot{\varepsilon}$ *i.e.* bone behaves differently under different mechanical loading conditions. An increase in Young's modulus $E$ and an increase in ultimate strength $\sigma_{ult}$ was reported by [17],[18],[19],[20] and [21]. A more interesting fact is that the strain at fracture $\varepsilon_f$ decreases with an increase in strain rate [17],[22].

Similar to the mechanical properties, bone had also been studied through FE simulations for years now. The most commonly implemented constitutive law for cortical bone is elastic-plastic [23],[24]. We can

see the use of elastic-plastic consitutitve law for trabecular bone in [27],[28]. Yet in contrast, there is evidence of using foam like constitutive laws for trabecular bone [12],[25],[26]

In this study, we propose an elasticviscoplastic constitutive law with isotropic hardening for cortical bone and an elasticviscoplastic constitutive law with kinematic hardening for trabecular bone. The constitutive law is coupled to an external path dependent damage law that is capable of considering non linear damage accumulation, reduction in rigidity through continuum damage mechanics, and strain rate effects on fracture strain.

# 2 Material and Methods

## 2.1 Experimental Procedure

The experimental tests were carried using a modified Split Hopkinson Pressure Bar (SHPB) setup for studying the behavior of material under dynamic three point bending. The principle of SHPB tests is to generate a compressive stress pulse through an impact of a striker (preferably of same material as bars) launched at the input bar. This compressive waves propagates ($\varepsilon_{inc}(t')$) along the length of input bar. Once the wave arrives at input bar sample interface, a part of it is reflected and a part of it is transmitted to the output bar(s) through the sample. The amount of wave reflected ($\varepsilon_{ref}(t')$) and transmitted ($\varepsilon_{tr1}(t')$ and $\varepsilon_{tr2}(t')$), depends on the difference in the mechanical impedance of bar and sample. Since the signals are acquired at a known distance form the interfaces, a time and space shifting procedure is required to differentiate these three waves. This includes the definition of arrival time for the incident wave pulse at the input bar-sample interface and then expressing all strain signals to the relative time (see Eq. 1) as such they were measured at the interface.

$$t = t' - t_0'$$ (1)

If the stress magnitudes in the bar are below yield limit of the bar material, then the plane wave formula is applicable. This formula leads to the dynamic variables used for describing the response of the sample *i.e.* Force at interfaces ($F_{inp}, F_{out1}, and F_{out2}$), velocity at interfaces ($v_{inp}, v_{out1}, and v_{out2}$), displacements at interface ($u_{inp}, u_{out1}, and u_{out2}$) expressed from Eq. 2 to Eq. 10

The porcine rib samples were brought from a local butcher and the surrounding muscles and tissues were removed prior to experiments. The experimental setup consists of a striker, an input bar (3 m long) and two output bars (1.75 m long). The bars of SHPB setup were made of nylon in order to adapt for the impedance difference between bars and rib sample. The anterior and posterior extremities of rib were sanded to establish a planar contact at the output bar-sample interface.

$$F_{inp} = A_b E_b \left[ \varepsilon_{inc}(t) + \varepsilon_{ref}(t) \right] \tag{2}$$

$$F_{out1} = A_b E_b \varepsilon_{tr1}(t) \tag{3}$$

$$F_{out2} = A_b E_b \varepsilon_{tr2}(t) \tag{4}$$

$$v_{inp} = -c_b \left[ \varepsilon_{inc}(t) - \varepsilon_{ref}(t) \right] \tag{5}$$

$$v_{out1} = -c_b \varepsilon_{tr1}(t) \tag{6}$$

$$v_{out2} = -c_b \varepsilon_{tr2}(t) \tag{7}$$

$$u_{inp} = \int_0^t v_{inp} dt \tag{8}$$

$$u_{out1} = \int_0^t v_{out1} dt \tag{9}$$

$$u_{out2} = \int_0^t v_{out2} dt \tag{10}$$

## 2.2   Numerical Rib Geometry

The numerical porcine rib sample was generated from the contours of DICOM images obtained through High Resolution-peripheral Quantitative Computed Tomography (HR-pQCT) scans. The porcine rib samples brought from a local butcher were soaked in saline solution, stored in a refrigerator at and, carefully defatted prior to CT scans. The raw DICOM image data were the imported to ScanIP module of Simpleware (Synopsys) for image processing, visualization and geometry generation of rib segments. A Five-sample calibration phantom with $K_2HPO_4$ and $H_2O$ densities was placed below the ribs in the course of scan. The raw linear attenuation data $\mu$ were converted to normalized data $GS$, expressed in Hounsfield Units using the following relation

$$GS \, [\text{HU}] = 1000 \left( \frac{\mu_b - \mu_w}{\mu_w - \mu_a} \right); \, \mu_w = 0; \mu_a = -1000; \tag{11}$$

here, $\mu_b$, $\mu_w$, and $\mu_a$ are $\mu$ values of bone, water, and air respectively.

In order to test the influence of different independent variables on the mechanical properties of bone, three different densities were calibrated :

1. Apparent Dry Density $\rho_{app}$, determined from the hypothesis presented by [29]. Firstly, the effective density $\rho_{eff}$ (Eq. 12)[1]. Once $\rho_{eff}$ is obtained, the $\rho_{app}$ was interpolated to $GS$ through a linear relation as in Eq. 13

$$\rho_{eff} \, [\text{kg.m}^{-3}] = 0.523 GS + 1000 \tag{12}$$

$$\rho_{app} \, [\text{kg.m}^{-3}] = 1.207 GS \tag{13}$$

2. Equivalent Mineral Density $\rho_{eqm}$. The $\rho_{eqm}$ was found from $GS$ values through the following equation

$$\rho_{eqm} \, [\text{kg.m}^{-3}] = 0.6452 GS + 0.487 \tag{14}$$

---

1. density of the sample including the bone marrow and fluids

3. Apparent Ash Density $\rho_\alpha$. Two methods were followed obtain $\rho_\alpha$ of porcine rib

   (a) form $\rho_{eqm}$, through Eq.

$$\rho_\alpha(\rho_{eqm}) \ [\text{kg.m}^{-3}] \ = \ 1.27\rho_{eqm} + 0.0452 \tag{15}$$

   (b) based on the relation of $\rho_\alpha$ with $\rho_{app}$, proposed by [15] as expressed as in Eq. 16 and Eq. 17

$$\rho_\alpha(\rho_{app}) \ [\text{kg.m}^{-3}] \ = \ 0.522\rho_{app} + 0.007; \ for \ \rho_{app} < 1000 \ \text{kg.m}^{-3} \tag{16}$$

$$\rho_\alpha(\rho_{app}) \ [\text{kg.m}^{-3}] \ = \ 0.779\rho_{app} - 0.250; \ for \ \rho_{app} \geq 1000 \ \text{kg.m}^{-3} \tag{17}$$
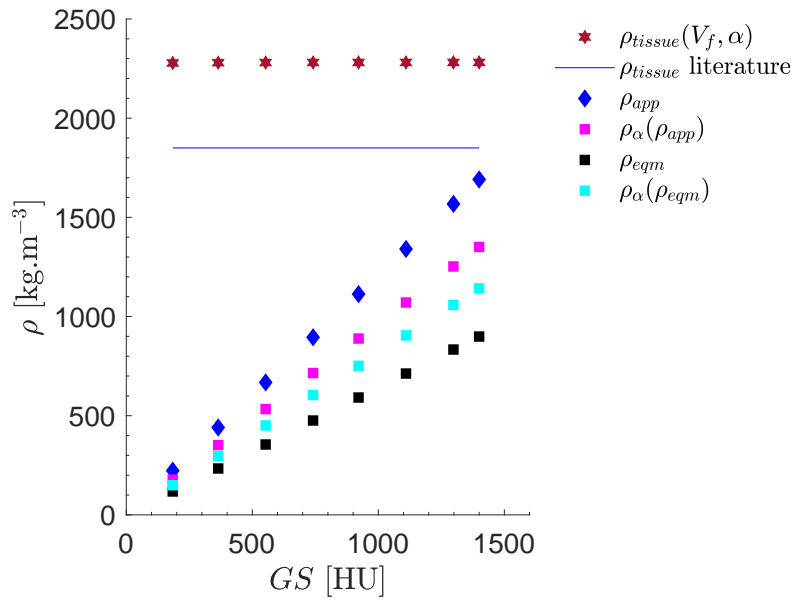


FIGURE 1 – Different density measures for porcine rib

## 2.3 Mechanical properties of bone

As said in introduction, the mechanical properties of rib constituents were determined using either single variable power law regression (Model 1a, 1b and 1c) or two variable power law regression (Model 2). These models predict mechanical properties such as Young modulus ($E$), Yield strength in compression and tension ($\sigma_{yC}$) and ($\sigma_{yT}$), Ultimate strength in compression and tension ($\sigma_{uC}$) and ($\sigma_{uT}$) respectively.

### 2.3.1 Single variable models

These models consider only one independent variable either $\rho_{app}$ (model-1a) or $\rho_\alpha$ (model-1b and model-1c).

**Model-1a**
The Model-1a is based on the hypothesis that $\rho_{app}$ is the only variable influencing the mechanical properties of bone. Since the porcine rib has both cortical and trabecular bone, corresponding porosity $Po$

values were calculated as follows

$$V_{f\,app} = \frac{\rho_{app}}{\rho_{tissue}} \tag{18}$$

$$Po_{app} = \left(1 - V_{f_{app}}\right) \times 100 \tag{19}$$

The $\rho_{tissue}$ used in Eq. 18 was considered as $1850\,\text{kg.m}^{-3}$ (same for both cortical and trabecular bone), that is represented as $\rho_{tissue}$ literature in Fig. 1. Corresponding power law regression equations available in literature were used for cortical and trabecular bone constituents based on $Po_{app}$ (see Tab. 1)

| Property | Cortical Bone | Trabecular Bone |
|---|---|---|
| Young's Modulus $E_{app}$, [MPa] | $1.109 \times 10^{-6}\,\rho_{app}^{3.09}$ | $0.5903\,\rho_{app}^{1.20}$ |
| Compressive Strength $\sigma_{uC\,app}$, [MPa] | $1.659 \times 10^{-4}\,\rho_{app}^{1.88}$ | $8.534 \times 10^{-4}\,\rho_{app}^{1.53}$ |
| Tensile Strength $\sigma_{uT\,app}$, [MPa] | $1.61 \times 10^{-4}\,\rho_{app}^{1.88}$ | $8.201 \times 10^{-4}\,\rho_{app}^{1.07}$ |
| Compressive Yield $\sigma_{yC\,app}$, [MPa] | $1.442 \times 10^{-4}\,\rho_{app}^{1.85}$ | $5.167 \times 10^{-4}\,\rho_{app}^{1.60}$ |
| Tensile Yield $\sigma_{yT\,app}$, [MPa] | $3.064 \times 10^{-4}\,\rho_{app}^{1.67}$ | $7.5686 \times 10^{-3}\,\rho_{app}^{1.04}$ |

TABLE 1 – Power law regression equations used for apparent mechanical properties (Model-1a)

**Model-1b**

In contrast to Model-1a, this model uses the apparent ash density obtained from [15] $\rho_\alpha(\rho_{app})$ as independent variable. The mechanical properties were obtained though the equations given below

$$E_{\alpha(\rho_{app})}\,[\text{GPa}] = 3.284 \times 10^{-6}\rho_\alpha^{1.92} \tag{20}$$

$$\sigma_{uC\alpha(\rho_{app})}\,[\text{MPa}] = 4.399 \times 10^{-5}\rho_\alpha^{2.27} \tag{21}$$

$$\sigma_{uT\alpha(\rho_{app})}\,[\text{MPa}] = 3.079 \times 10^{-5}\rho_\alpha^{2.27} \tag{22}$$

**Model-1c**

This model uses the apparent ash density obtained from $\rho_{eqm}$ as independent variable. The mechanical properties were obtained though the equations given below

$$E_{\alpha(\rho_{eqm})}\,[\text{GPa}] = 3.284 \times 10^{-6}\rho_\alpha^{1.92} \tag{23}$$

$$\sigma_{uC\alpha(\rho_{eqm})}\,[\text{MPa}] = 4.399 \times 10^{-5}\rho_\alpha^{2.27} \tag{24}$$

$$\sigma_{uT\alpha(\rho_{eqm})}\,[\text{MPa}] = 3.079 \times 10^{-5}\rho_\alpha^{2.27} \tag{25}$$

### 2.3.2 Two variable model

The two variable model used in this study was based on [16], that considers both the volume fraction $V_f$ and ash fraction $\alpha$ of the porcine rib sample. The assumption proposed by [16] is *the ash fraction and volume fraction of bone influence the mechanical properties*, therefore, $\rho_{tissue}$ in this model was interpolated through Eq.26 as opposed to a constant value of $1850\,\text{kg.m}^{-3}$ in Model-1a.

$$\rho_{tissue} = \frac{\rho_{app}}{1.41 + 1.29\alpha} \tag{26}$$

Since $\rho_{tissue}$ is not constant, the $V_f$ does not have the same evolution for different $GS$ values as of Model-1a, thereby changing the $Po$ values. The mechanical properties in this model were obtained through the following equations

$$E_{\alpha,V_f} \, [\text{GPa}] \; = \; 84.37 \, V_f^{2.58} \alpha^{2.74} \tag{27}$$

$$\sigma_{uC\alpha,V_f} \, [\text{MPa}] \; = \; 794.33 \, V_f^{1.92} \alpha^{2.79} \tag{28}$$

$$\sigma_{uT\alpha,V_f} \, [\text{MPa}] \; = \; 556.00 \, V_f^{1.92} \alpha^{2.79} \tag{29}$$

### 2.3.3 Comparison of regression models

In order to make sure which hypothesis shall be considered for the material properties of bone, the results of single variable model and two variable model were compared and verified with the element distribution in the numerical rib sample.

First of all, the different density measures obtained through all these models were compared. The ash density of model-1b $\rho_{\alpha}(\rho_{app})$ is greater than that of model-1c $\rho_{\alpha}(\rho_{eqm})$. This is due to the sample origin used for correlation *i.e.* the data presented by [15] was obtained from pooling data of human femur and human vertebrae, whereas, $\rho_{\alpha}(\rho_{eqm})$ of Model-1c was specific to porcine ribs. This shows the ash fraction varies for different species, thereby explaining the overestimation of density data.

Secondly, the volume fractions and porosity from Model-1a and Model-2 $V_{f_{app}}$,$Po_{app}$ and $V_f(\alpha)$, $Po(\alpha)$ were compared. This again proved that the ash fraction had a tendency of over estimating the values.

Lastly, estimated mechanical properties common to all 4 power law regression models (Young modulus, ultimate strength in compression and tension) were compared. Regarding the mechanical properties, following conclusions can be drawn

- The young's modulus obtained thorough apparent density and two variable model are of similar range and are largely high to those obtained from apparent ash density based models (see Fig. 2a).
- The ultimate properties are highly influenced by $\alpha$ or $\rho_{\alpha}$ as it can be seen in Fig. 2b. Even though the model 2 considers $\alpha$, it does produce results similar to those obtained from apparent density.

We can conclude that the ash content in bone has a strong positive correlation on strength of bone and a negative correlation on the initial elastic behavior of bone. The reason for this influence in particular for human ribs or its biological surrogates is yet to be explained.
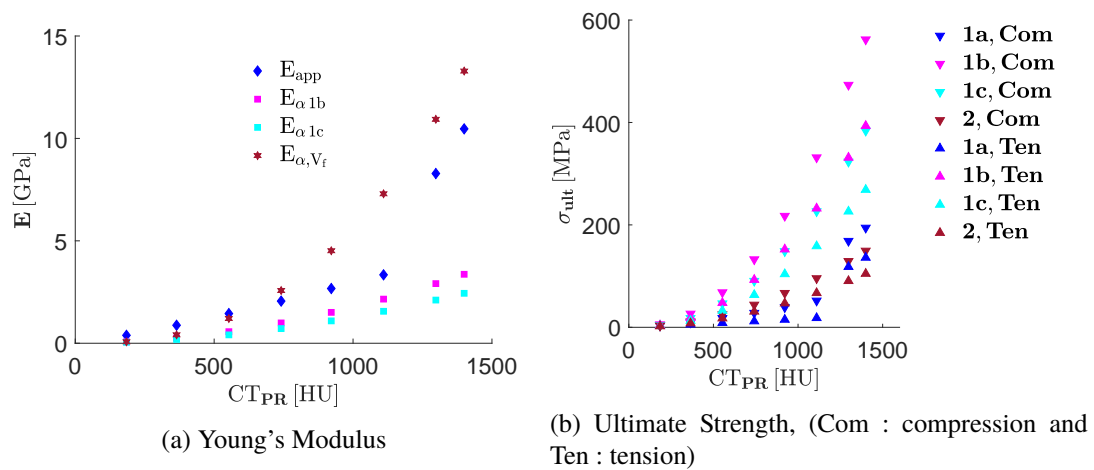
(a) Young's Modulus

(b) Ultimate Strength, (Com : compression and Ten : tension)

FIGURE 2 – Comparison of mechanical properties for porcine rib

Unfortunately, there is a lack of data on the influence of $\alpha$, $\rho_\alpha$ or two variable models on $\sigma_y$.

The constituents of porcine rib, obtained from model 1a and model 2 were compared with the element distribution of numerical rib sample based on porosity values. It is clearly seen that $Po_{app}$ is in strict accordance with the element distribution in contradiction to those obtained by $Po_{\alpha,V_f}$ of model 2. This element distribution is shown in figure below and corresponding density and porosity values.
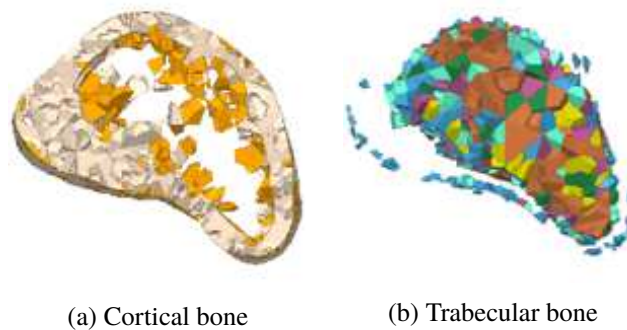


(a) Cortical bone

(b) Trabecular bone

FIGURE 3 – Element distribution in porcine rib sample

The properties obtained from apparent density are in accordance with that used by previous authors for human rib. The comparison in presented below

| Author | Origin | Bone | $\rho, \mathrm{kg.m^{-3}}$ | $E, \mathrm{GPa}$ | $\sigma_y, \mathrm{MPa}$ |
|---|---|---|---|---|---|
| [30] | Human | Cortical | 2000 | 13 | 150 |
| | Human | Trabecular | 1000 | 2.4 | 2 |
| [27] | Human | Cortical | 2000 | 11.5 | 88 |
| | Human | Trabecular | 1000 | 0.04 | 2.2 |
| [28] a | Human | Cortical | 2000 | 11.03 | 98.98 |
| | Human | Trabecular | 1000 | 0.04 | 1.8 |
| [28] b | Human | Cortical | 2000 | 12.38 | 82.36 |
| | Human | Trabecular | 1000 | 0.04 | 1.8 |
| This study | Porcine | Cortical | 1630.00 | 9.37 | 70.876 |
| | Porcine | Trabecular | 779.92 | 1.80 | 24.48 |

TABLE 2 – Comparison of average porcine rib apparent properties with human rib

These data prove that either $V_f$ or $\rho_{app}$ based regression models are efficient and reliable for having a decent insight on mechanical properties given that it is correctly correlated to $GS$.

## 2.4   FE Simulations

The FE simulations presented in this study were carried out at experimental scale. An elastic constitutive model was chosen for bars. The striker was given an initial velocity of $17.40$ $[\mathrm{m.s^{-1}}]$.

A good constitutive law for bone material must consider the strain rate effects. As proven by [31] that at higher strain rates, the strain rate has more effects on the post yield regime and the use of elastic-viscoplastic constitutive law by [27] proves that the elastoviscoplastic constitutive law is adaptable for bone material. Therefore, a classic elastic plastic constitutive law was modified to consider the strain rate effects on post yield behavior through the cowper-symmonds model, that can be expressed as

$$\frac{\sigma_{yd}}{\sigma_{y0}} \; = \; 1 \; + \; \left(\frac{\dot{\varepsilon}}{C}\right)^{1/P} \tag{30}$$

here, $\sigma_{yd}$ is the strain sensitive yield stress, $\sigma_{y0}$ is the initial yield stress, $\dot{\varepsilon}$ is the strain rate, $C$ and $P$ are cowper-symmonds parameters. The $\sigma_{y0}$ is identified as the tensile yield stress presented in Tab. 2. The cowper-symmonds parameters are adapted from [27] and are specified here for the sake of clarity $C = 2.5$ GPa and $P = 7.0$. The cortical and trabecular bone were supposed to obey isotropic and kinematic hardening respectively as found in previous studies.

In order to simulate the progressive nature of fracture propagation and damage accumulation, an external damage law was coupled to the constitutive law. This law is incremental and stress-state dependent and is capable of considering the reduction in load carrying capacity and effects of strain rate. This model is based on the works of [32] and [33]. The dependency on stress state is considered through stress triaxiality as follows

$$\eta \; = \; -\frac{\frac{1}{3}\mathrm{tr}\,\bar{\bar{\boldsymbol{\sigma}}}}{\sigma_{eq}} \tag{31}$$

where : $\frac{1}{3}\mathrm{tr}\,\bar{\bar{\boldsymbol{\sigma}}}$ is the hydrostatic pressure (average of the $\bar{\bar{\boldsymbol{\sigma}}}$ stress tensor trace) and $\sigma_{eq}$ is the equivalent stress.

The relation between the fracture strain $\varepsilon_{fd}$ and triaxiality $\eta$ – Eq. (31) – is given in the form of an input

curve plotted in Fig. 4a.

In this study, the static fracture strain $\varepsilon_{fs}$ value is $2 \times 10^{-2}$ m/m for cortical and $3 \times 10^{-2}$ m/m for trabecular bone. To approach the realistic fracture and propagation behavior using our damage model, the influence of strain rate $\dot{\varepsilon}$ on the fracture strain $\varepsilon_{fd}$ was implemented by an equation from [22] as follows :

$$\frac{\varepsilon_{fd}}{\varepsilon_{fs}} = A - B \operatorname{Ln}\dot{\varepsilon} \tag{32}$$

where $A = 0.63$. Five different values of $B = 1.25 \times 10^{-2}$. The corresponding $\varepsilon_{fd}/\varepsilon_{fs}$ vs $\dot{\varepsilon}$ input curve is plotted in Fig. 4b.
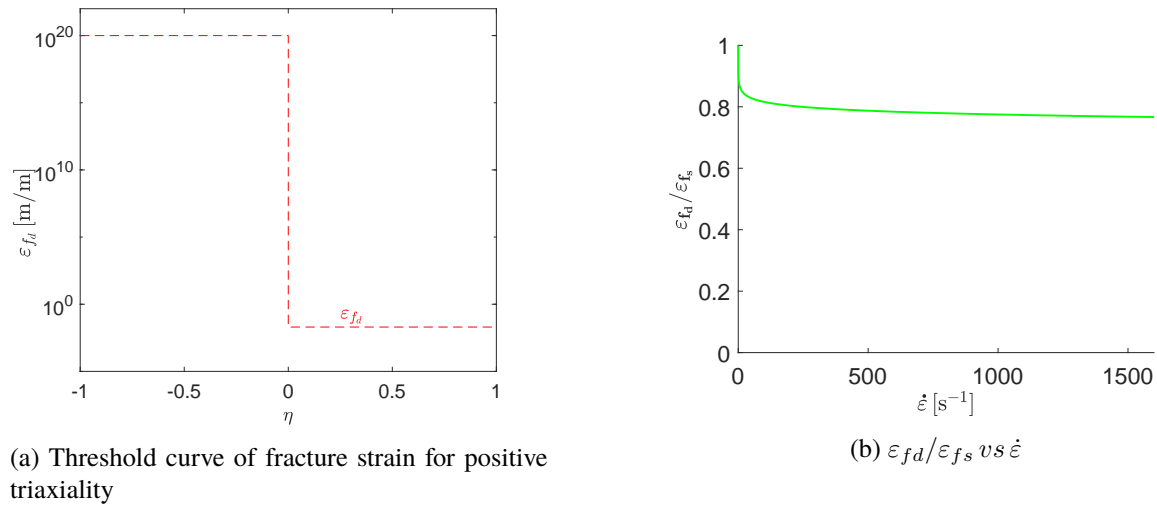


(a) Threshold curve of fracture strain for positive triaxiality

(b) $\varepsilon_{fd}/\varepsilon_{fs} \, vs \, \dot{\varepsilon}$

FIGURE 4 – Input curves of damage law

Note that the static fracture strain provided by [22] is $0.86 \times 10^{-2}$ m/m, which corresponds to a quasi-static strain-rate of $3.18 \times 10^{-3} \ \mathrm{s}^{-1}$. Similarly, in the present study Eq. (32) is not applicable for $\dot{\varepsilon}$ lower than $3.00 \times 10^{-3} \ \mathrm{s}^{-1}$, which are quasi static. For all values $0 \ \mathrm{s}^{-1} \leq \dot{\varepsilon} \leq 3.00 \times 10^{-3} \ \mathrm{s}^{-1}$, a linear approximation is applied so that $\varepsilon_{fd}/\varepsilon_{fs} = 1$ at $\dot{\varepsilon} = 0 \ \mathrm{s}^{-1}$.

The increments in damage $\Delta D$ is expressed in terms of plastic strain $\Delta\varepsilon_p$ and triaxility $\eta$ as follows :

$$\Delta D = \frac{n}{\varepsilon_{fd}(\eta, \dot{\varepsilon})} D^{(1-1/n)} \Delta\varepsilon_p \tag{33}$$

The damage exponent $n$ is to differentiate between linear and non-linear damage accumulation.

The reduction in load carrying capacity due to an increase in damage is taken into account through a modified equation of Lemaitre's effective stress principle :

$$\sigma = \tilde{\sigma} (1 - D^m) \tag{34}$$

When the damage $D$ reaches 1.0, fracture occurs and the Gaussian integral point of the corresponding element no longer exists in the calculation.

The damage exponent $n$ values for cortical and trabecular bone were 1.25 and 2.0 respectively. Unfortunately, the lack of database on the fading exponent $m$ for bone had led us to use $m = 1.0$.

When the yield stress is reached damage $D$ starts to accumulate according to Eq. (33). The fracture strain $\varepsilon_{fd}$ influences this accumulation. The more $\varepsilon_{fd}$ decreases with increasing strain-rate, more drastic will be the increase in damage accumulation $\Delta D$ and in $\Delta \varepsilon_p$.

The ultimate damage value $D = 1$ is reached through the non-linear coupling between damage $D$, fracture strain $\varepsilon_{fd}(\eta, \dot{\varepsilon})$, plastic strain $\varepsilon_p$ and softening. When $D = 1$, the corresponding element is removed from the structure, thereby initiating the crack propagation until fracture.

The strain rate influence on the post-yield behavior is also clear on the energy $W$ absorbed by the structure. The more rapid is the decrease $\varepsilon_{fd}$ with respect to $\dot{\varepsilon}$, less is the energy absorbed.

## 3    Results and Discussions

The results were analyzed in terms of force-time response and force-displacement response.

**Experimental results**

The forces in Fig. 5a were obtained through Eq. 2, Eq. 3 and Eq. 4 respectively. This response was classed into the category "Fracture before dynamic equilibrium" *i.e.* fracture of rib long before a dynamic equilibrium is established between $F_{inp}$ and $(F_{out1} + F_{out2})$. The time taken by other porcine rib samples to establish dynamic equilibrium was $\approx 6.00 \times 10^{-4}$s. The rupture of rib is characterized by a brutal decrease in force, occurs at $\approx 5.20 \times 10^{-4}$s.

On the other hand, the structural response of rib was analyzed by force-displacement curves. Three different corridors were established with relative interface velocities and the Corridor-3 is shown in Fig. 5b which represent a group of force-displacement curves enclosed in maxima and minima of all curves of corresponding corridor.
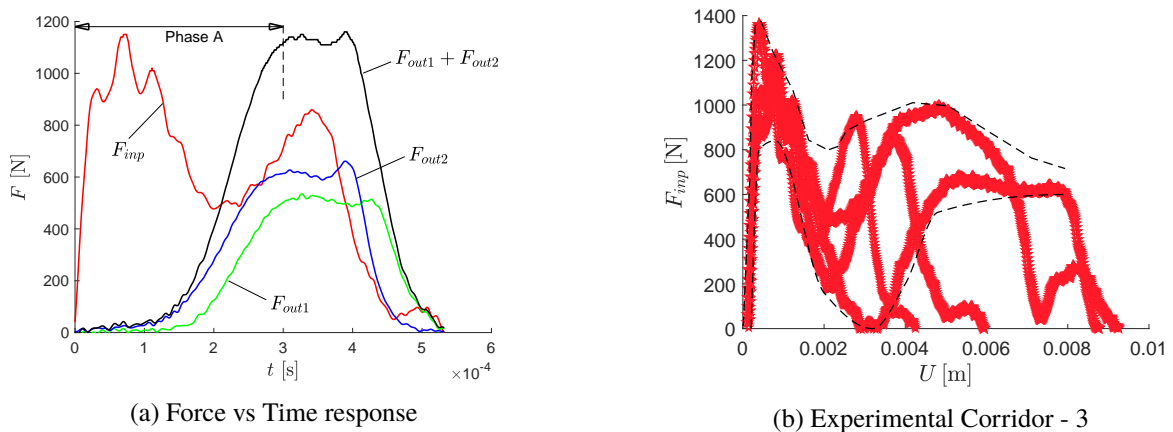


(a) Force vs Time response                     (b) Experimental Corridor - 3

FIGURE 5 – Experimental Results

**Numerical results**

The numerical responses were also obtained through the same shifting procedure of the numerical strain signal. The striker was given a velocity of $17.40\,\mathrm{m.s^{-1}}$ to simulate a similar experimental case of fracture

before equilibrium. The numerical responses are shown in figure below compared to the corresponding experimental results. Following deductions can be drawn,

1. A keen observation to the $\varepsilon_{inc}$ and $\varepsilon_{ref}$, reveals that there is a slight difference between numerical and experimental signals. On the other hand, the difference in the transmitted strain signals can be explained by the difference in geometry. Yet, the numerical interface velocities and displacements are almost similar to that of experimental.

2. The numerical displacement of output interface 2 shows a peculiar response. It is clear that it superposes with experimental signal till $t \approx 500 \times 10^{-4}$s. Beyond this point of time the magnitude of $u_{out2}$ Num is greater than $u_{out1}$ Exp, that can be explained by the loss of contact between the sample and output bar interface 2. The increase in displacement beyond this time represents the rigid displacement of output bar.



(a) incident and reflected waves   (b) transmitted waves

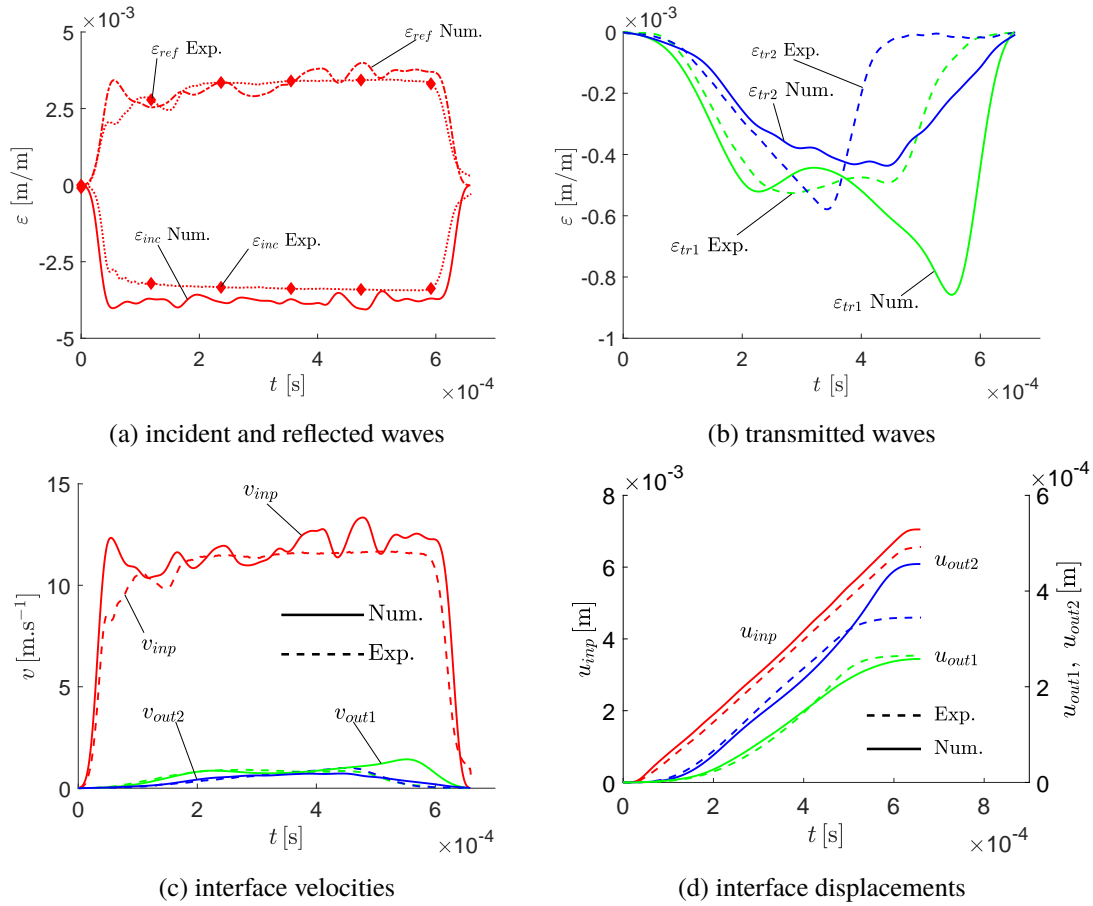(c) interface velocities   (d) interface displacements

FIGURE 6 – Experimental and Numerical strain, interface velocities and displacements

The numerical force-displacement response is shown in figure below. Initially, the structure behaves as an elastic material (till $t \approx 0.75 \times 10^{-4}$ s). During this period of time, the response depends on material properties and the stiffness distribution. Beyond this time, the force starts to increase till it reaches the maximum value and decreases till $t \approx 2.05 \times 10^{-4}$ s. This is followed by an increase in force, which represents the reflection of waves from output interface. The second decrease in force starts to occur when a crack appears in macro scale thereby proving the reduction in force carrying capacity of the rib until rupture at $t \approx 5.00 \times 10^{-4}$ s or $U \approx 5.00 \times 10^{-3}$ m.
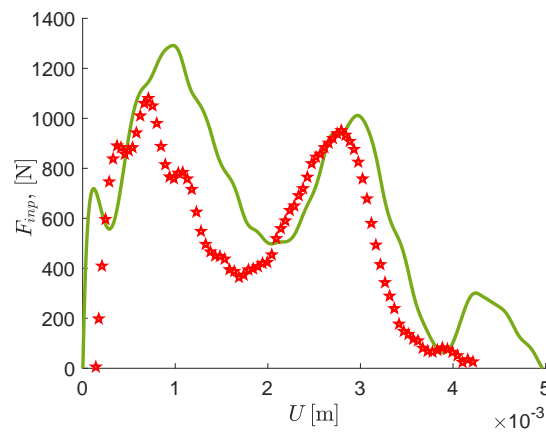
FIGURE 7 – Comparison of Numerical response to experimental response

# 4  Conclusions

Dynamic three point bending tests using the split hopkinson pressure bar on rib was successfully implemented to have insights on fracture of ribs.

Different power law regression models were tested. The apparent density was the one that gave reliable results. The power law regression models with apparent ash density or ash fraction had a tendency to over estimate the ultimate properties of porcine rib. Moreover, the average apparent properties of porcine rib constituents are in good accordance with those of human ribs. This proves that the choice of porcine rib as human surrogates is biologically reliable.

The numerical results in this study prove that the FE model presented in this study is pertinent. The strain rate effects in behavior and damage till rupture were successfully taken into account. Even though the FE model results are coherent with that of experiments, optimization of damage law parameters through uni axial tensile test data could further improve the predicting capability of the model.

# Références

[1]  K. Horst,H. Andruszkow, C.D. Weber, M. Pishnamaz, C. Herren, Q. Zhi, M. Knobe, R. Lefering, F. Hildebrand, H.C Pape, Thoracic trauma now and then : A 10 year experience from 16,773 severely injured patients PLoS ONE, 12 (2017).

[2]  Y. Arunan, B. Roodenburg, Chest Trauma, Anaesthesia & Intensive Care Medicine, 18 (2017) 390–394.

[3]  C.D Dewar, S.M. Tarrant, K.L. King and E.J. Balogh, Changes in the epidemiology and prediction of multiple-organ failure after injury, The Journal of Trauma and Acute Care Surgery, 74 (2013) 774–779.

[4]  N.Burnside , K.McManus, Blunt thoracic trauma, Surgery (Oxford), 32 (2014) 254–260.

[5]  H.Fallouh, R. Dattani-Patel and S.Rathinam, Blunt thoracic trauma. Surgery (Oxford), 35 (2017) 262–268.

[6]  S.L.Schoell, A.A.Weaver,N.A.Vavalle, J.D.Stitzel, Age- and sex-specific thorax finite element model development and simulation, Traffic Injury Prevention, 16 (2015) 57–65.

[7]  E. Haug, H.Y.Choi, S.Robin and M.Beaugonin, Computational Models for the Human Body, Handbook of Numerical Analysis, Elsevier, 12 (2004) 231-542.

[8]  P.J. Arnoux, S. Jooneknidt, L.Tholon and K. Kayvantash, Radioss finite element model of the Thor dummy, International Journal of Crashworthiness 8 (2003) 529–541.

[9]  T.Maeno and J.Hasegawa, Development of a Finite Element Model of the Total Human Model for Safety (THUMS) and Application to Car-Pedestrian Impacts, SAE International (2001).

[10]  S. Robin, HUMOS : HUman MOdel for Safety - A joint effort towards the development of refined human like car occupant models in :, Proceedings of 17th International technical conference on the enhanced safety of vehicles, (2001).

[11]  D.R. Carter, W.C. Hayes, Compressive behavior of bone as a two-phase porous structure, Journal of Bone Joint Surgery, 59 (1977) 954–962.

[12]  L.J. Gibson, Mechanical behavior of cancellous bones, Journal of Biomechanics, 18 (1985) 317–328.

[13]  J.H. Keyak, I.Y. Lee, H.B. Skinner, Correlations between orthogonal mechanical properties and density of trabecular bone : use of different densitometric measures, Journal of Biomedical Materials Research, 28 (1994) 1329–1336.

[14]  G.P. Vose, A.L. Kubala, Bone strength-its relationship to X-ray-determined ash content, Human Biology, 31 (1959) 261–270.

[15]  T.S. Keller, Predicting the compressive mechanical behavior of bone, Journal of Biomechanics, 27 (1994) 1159–1168.

[16]  C.J. Hernandez, G.S Beaupré, T.S. Keller, D.R. Carter, Influence of bone volume fraction and ash fraction on bone strength and modulus, Bone, 29 (2001) 74–78.

[17]  J.H. McElhaney, Dynamic response of bone and muscle tissue, 1966, Journal of Applied Physiology, 21 (1966) 1231–1236.

[18]  R.D. Crowninshield, M.H. Pope, Response of compact bone in tension at various strain rates, Annals of Biomedical Engineering, 2 (1974) 217–225.

[19] J.D. Currey, The effects of strain rate, reconstruction and mineral content on some mechanical properties of bovine bone, Journal of Biomechanics, 8 (1975) 81–86.

[20] T.M. Wright, W.C. Hayes, Tensile testing of bone over a wide range of strain rates : effects of strain rate, microstructure and density, Medical & Biological Engineering, 14 (1976) 671–680.

[21] U. Hansen, P. Zioupos, R. Simpson, J.D Currey, D. Hynd, Effects of strain rate on mechanical properties of human cortical bone, Journal of Biomedical Engineering, 130 (2008).

[22] J.L. Wood, Dynamic response of human cranial bone, Journal of Biomechanics, 4 (1971) 1–12.

[23] D. Garcia, Elastic-plastic damage laws for cortical bone, PhD. Thesis, Ecole Polytecnique Fédérale de Laussane, 2006.

[24] J. Pavier, Contribution à la compréhension des phénomènes physiques lors de l'impact d'un corps sur un modèle de structure biologique. Thèse, Université d'Orléans, 2013.

[25] N. Kelly, J.P. McGarry, Experimental and numerical characterization of the elastic-plastic properties of bovine trabecular bone and a trabecular bone analogue, Journal of Mechanical Behavior of Biomedical Behavior, 9 (2012) 184–197.

[26] M. Karkar, Personnalisation morpho-mécanique de la voûte crânienne humaine à différentes vitesses de sollicitations, Thèse, Université de Valenciennes, 2017.

[27] Z. Li, M.W. Kindig, J.R. Kerrigan, C.D. Untaroiu, D. Subit, J.R. Crandall, R.W. Kent, Rib fractures under anterior-posterior dynamic loads : Experimental study and Finite Element Simulations, Journal of Biomechanics, 24 (2010) 228–234.

[28] K. Yates, C. Untaroiu, Subject specific modeling of human ribs : Finite Element simulations of rib bending tests, mesh sensitivity, model testing with data from coupon tests, In : Proceedings of 15th international LS-Dyna User's Conference, 2018 ;

[29] W.R. Taylor, E. Roland, H. Ploeg, D. Hertig, R. Klabunde, M.D. Warner, M.C. Hobatho, L. Rakotomanana, S.E. Clift, Determination of orhtotropic bone elastic constants using FEA and modal analysis, Journal of Biomechanics, 35 (2002) 767–773,

[30] E. Charpail, Analyse du comportement mécanique des côtes humaines en dynamique, Thèse, École National de Supérieur d'Arts et Métiers , 2006,

[31] P. Zioupos, U. Hansen, J.D. Currey, Microcracking damage and the fracture process in relation to strain rate in human cortical bone tensile fracture, Journal of Biomechanics, 41 (2008) 2932–2939,

[32] N. Frieder, F. Markus, H. André, Considering damage history in crash-worthiness simulations, In : Proceedings of 7th international LS-Dyna User's Conference, 2009 ;

[33] A. Fillipe, F. Markus, H. André, On the prediction of damage and failure in LS-Dyna : a comparison of GISSMO and DIEM, In : Proceedings of 13th international LS-Dyna User's Conference, 2014 ;